Finite Element Computation for Solving Pulsatile Blood Flow: Relevance in Assessing the Flow Dynamics in Abdominal Aortic Aneurysms

Vijayajothi Paramasivam[1, 4C], Nenad Filipovic[2, 3], Kanesan Muthusamy[1], Mohammed Rafiq Abdul Kadir[4]

[1] *Faculty of Science & Technology, Open University Malaysia, Malaysia,*
[2] *Faculty of Mechanical Engineering, University of Kragujevac, Serbia,*
[3] *Harvard School of Public Health, Boston, USA,*
[4] *Medical Implant Technology Group (MEDITEG), Faculty of Biomedical Engineering & Health Science, Universiti Teknologi Malaysia, Malaysia*

Abstract

The objective of this paper is to present the mixed velocity-pressure (v-p) finite element method that solves the pulsatile blood flow in arteries. The solution exploits the Galerkin method and the fully implicit incremental-iterative procedure for the three-dimensional nonlinear finite element equations. This methodology is applied to model biological flows that are important in predicting growth and rupture risks in abdominal aortic aneurysms (AAA). The numerical technique was validated with the analytical solution of the Womersley model. Next, a physiologically realistic pulsatile blood flow waveform was imposed onto the idealized cylindrical arterial model and solved as a benchmark problem. The model represents a healthy abdominal aorta. This pulsatile condition simulates an *in vivo* aorta at rest. The numerical results were used to quantify clinically relevant flow dynamics that play a significant role in today's field of medical treatment planning and development of predictive methods via computational modelling for assessing common clinical problems such as AAAs.

Keywords: Three-dimensional finite element methods; Pulsatile flow dynamics; Abdominal aorta.

1.   Introduction

Abdominal aortic aneurysm (AAA) is a common clinical problem that requires determination of hemodynamic conditions and subsequent rupture prediction. AAAs, are aneurysms occurring in the abdominal part of the aorta, more specifically, between the renal bifurcation and the iliac branches. The main causes of aneurysm are arteriosclerosis and cystic medial degeneration, but also genetic disorder, malfunction of the aorta (i.e. biomechanical phenomenon), mycotic infections or arthritis can be a cause of aneurysm [1]. Another cause of aneurismal disorders mentioned by scientists is the loss of distensibility of the vessels.

C c Corresponding Author: P. Vijayajothi
Email: vjjothi@yahoo.com   Telephone: +607 2526931   Fax: +607 2541952

This pathologic condition has been found to affect 8.8% of the population over the age of 65 and if left untreated it may lead to rupture [2]. Although the size of the aneurysm and its rate of expansion are parameters widely associated with the risk of rupture, it is important to understand the flow dynamics of pulsatile flow in a healthy aorta and its flow implications under an aneurismal condition [3].

A fundamentally new approach in medical treatment planning and development of predictive methods in clinical applications is computational modelling. Mathematical models can help to interpret non-invasive monitoring techniques. The numerical methods used to study AAA development vary from one researcher to another. However, the finite element method is commonly used these days [4,5,6]. The key factor that determines the reliability of the finite element scheme is its stability. Generally, the finite element computation of incompressible flows involves two main sources of potential numerical instabilities associated with the Galerkin formulation of a problem. One source is due to the presence of advection terms in the governing equations, and can result in spurious node-to-node oscillations primarily in the velocity field. Such oscillations become more apparent for advection-dominated (i.e. high Reynolds number) flows and flows with sharp layers in the solution.

The other source of instability is due to using inappropriate combinations of interpolation functions to represent the velocity and pressure fields. These instabilities usually appear as oscillations primarily in the pressure field. In last decades a number of stabilization procedures have been developed to prevent potential numerical instabilities described above [7,8,9,10,11]. In order to guarantee the stability of the scheme, the finite elements for velocity and pressure need to be selected in a proper way to satisfy the inf-sup condition of Ladyzhenskaya-Babuska-Brezzi (LBB) condition [12].

On the finite element level, we consider solving a system of equations in a finite element space V_h x P_h, where V and P are velocity and pressure respectively. Here the parameter h usually refers to the mesh size. The stability properties of the finite element method based on V_h x P_h is determined by the inf-sup condition such that the inf-sup constant is;

$$\gamma_h := \overset{\inf}{0 \neq p \in P_h} \overset{\sup}{0 \neq v \in V_h} \frac{\int_\Omega p \, div v}{\|v\|1,\Omega \|p\|0,\Omega} > 0$$

where Ω is a polygonal domain. A finite element is called stable if there exists $\gamma > 0$ independent of h such that $\gamma_h \geq \gamma$ holds for any mesh of the domain Ω and for any mesh size $h > 0$. Similarly, a finite element is said to be stable for a mesh family if λ_h can be bounded by a positive number for any mesh of the mesh family. Therefore, with good approximation properties and finite element method can be stable.

We aim to derive a complete set of three-dimensional finite element equations arising from the mixed velocity-pressure (v-p) finite element method by implementing the Galerkin method and the fully implicit incremental-iterative procedure for solving the nonlinear Navier Stokes and continuity equations that represent blood as a viscous incompressible Newtonian fluid, that can be applied to solve pulsatile flow problems in arteries.

2. Methods
2.1. Governing equations

Except in tiny capillaries, the blood flow can be assumed to behave as a continuum, as well as incompressible, apart from severe pathological situations [13]. Although, in reality blood is a non-Newtonian suspension of cells in plasma, but it is reasonable to model it as a Newtonian fluid in vessels greater than approximately 0.5mm in diameter [14]. The

three-dimensional governing equations (momentum and continuity equations) of a viscous incompressible Newtonian fluid (blood) flow, using the indicial notations with the usual summation convention are, respectively,

$$\rho\left(\frac{\partial v_i}{\partial t} + v_j v_{i,j}\right) = \sigma_{ij,j} + f^{\,B}_{\,i} \tag{1}$$

$$v_{i,i} = 0 \tag{2}$$

where v_i is velocity of blood flow in direction x_i, and summation is assumed on the repeated (dummy) indices, i, j = 1, 2, 3. ρ, $\sigma_{ij,j}$ and f^B_i are the fluid density, fluid stress and body force, respectively. Its prescribed velocity on the surface S_1 and boundary force on the surface S_2 as the governing boundary conditions imposed onto equations (1) and (2) are, respectively,

$$v_i = \bar{v}_i\big|_{S_1} \tag{3}$$

$$\sigma_{ij} n_j = f^{\,S}_{\,i}\big|_{S_2} \tag{4}$$

where the fluid domain of interest S with its boundaries are given as;

$$S_2 \cup S_1 = S \text{ and } S_2 \cap S_1 = \varnothing \tag{5}$$

Next, a constitutive equation for the fluid stress for Newtonian fluid is introduced as;

$$\sigma_{ij} = -p\delta_{ij} + 2\mu\dot{e}_{ij} \tag{6}$$

where, p is the fluid pressure, μ is the dynamic viscosity of the fluid, $\dot{e}_{ij}$ is the tensor of velocity deformation, $\dot{e}_{ij} = \dfrac{1}{2}\left(\dfrac{\partial v_i}{\partial x_j} + \dfrac{\partial v_j}{\partial x_i}\right)$ and δ_{ij} is the Kronecker delta. Substituting equation (6) into equation (1) and subsequently applying equation (2) gives rise to the final form of the flow equation;

$$\rho\left(\frac{\partial v_i}{\partial t} + v_j v_{i,j}\right) = -p_{,i} + \mu v_{i,jj} + f^{\,B}_{\,i} \tag{7}$$

2.2. Pulsatile flow and boundary conditions

A physiologically realistic pulsatile blood flow simulating an *in vivo* cardiac cycle of the abdominal aorta section at rest was imposed at the inlet of the non-dilated aorta entry, d_{AA}, as shown in Figure 1 [15]. The mean Reynolds number, $Re_{mean}=4Q_{mean}/\pi \upsilon d_{AA}$ and peak Reynolds Number, $Re_{peak}=4Q_{peak}/\pi \upsilon d_{AA}$ of the pulsatile flow were 525 and 2325, respectively. The mean Reynolds number is based on the mean flow rate, Q_{mean} of a full cardiac cycle whereas the peak Reynolds number is based on the peak systolic flow rate, Q_{peak} of the pulsatile flow. The pulsatile flow consists of a pulse frequency, ω of 60beats/min, so that the Womersley number, $\alpha = 0.5 d_{AA}\sqrt{\omega/\upsilon} \approx 12$, where υ is the kinematic viscosity of blood which was taken to be 3.5mm^2/s.

At the inlet of the aorta, the pulsatile flow imposed is considered to be a fully developed flow in an infinitely long straight cylindrical tube model. All velocity components at the fixed vessel wall of the aorta model are prescribed as zero. The no-slip condition at the inner vessel wall was adopted. Along the symmetric plane of the model, the velocity components normal to this plane and the tangential stresses are imposed to be zero. At the outlet of the aorta, the normal and tangential stresses are set to be zero as well respectively (i. e. stress-free condition). Therefore, near the outlet of the aorta the solution differs from the solution in an infinitely long straight cylindrical tube model.
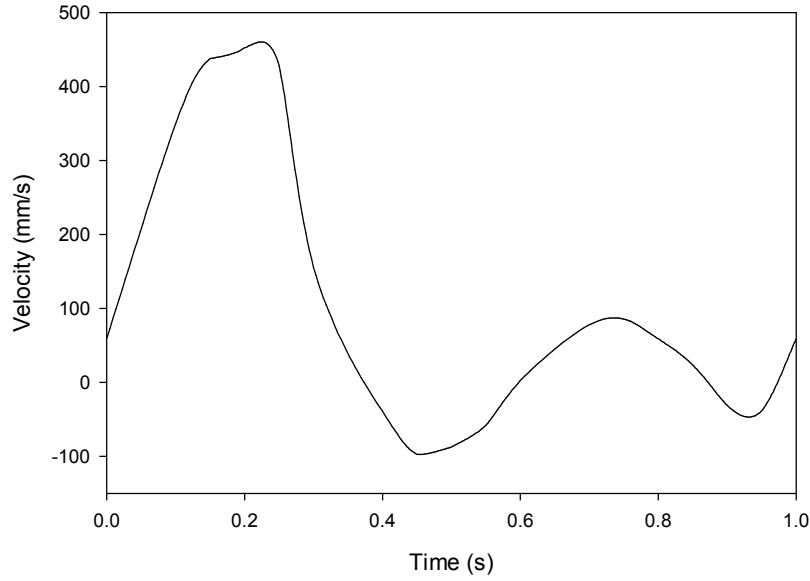
Figure 1. Pulsatile waveform imposed at the entry of the aorta

2.3. Finite element formulation

The advantage of the mixed velocity-pressure (v-p) formulation is that the pressure, velocity, velocity gradient and stress boundary conditions can be directly incorporated into the finite element matrix equations [12]. A 21/8 node 3D brick element was used for this three-dimensional analysis. 21 nodes were employed to interpolate the velocities and 8 nodes were employed to interpolate the pressure, hence, providing stable elements expressed by the inf-sup condition of Brezzi-Babuska. The finite element mesh of the model consists of 7,200 elements and 8,450 nodes, as shown in Figure 2.
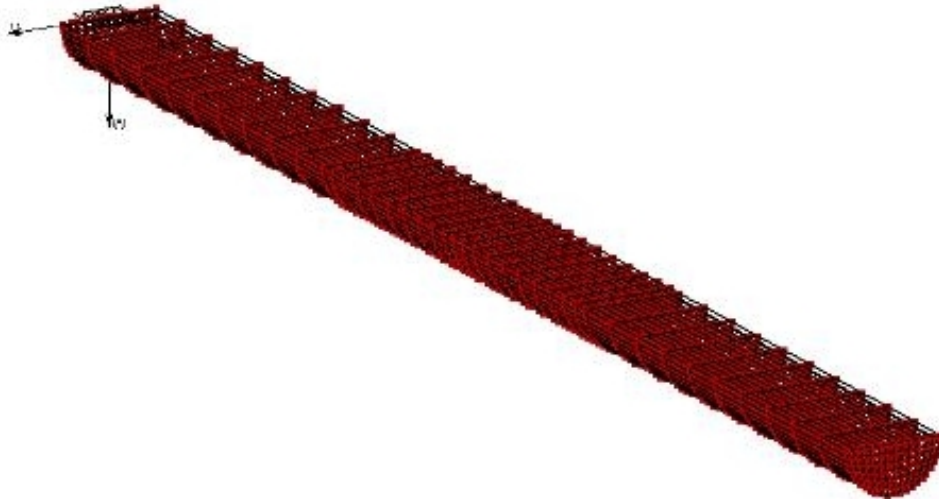

Figure 2. Finite element model of a straight cylindrical tube representing a healthy aorta

Applying the Galerkin method in equations (2) and (7) yields;

$$\int_V G_\delta v_{i,i} dV = 0$$

(8)

$$\rho \int_V H_\alpha \frac{\partial v_i}{\partial t} dV + \rho \int_V H_\alpha v_j v_{i,j} dV = -\int_V H_\alpha p_{,i} dV + \int_V \mu H_\alpha v_{i,jj} dV + \int_V H_\alpha f_i^B dV$$

(9)

Integrating by parts and transforming the volume to surface integral of equation (9) yields;

$$\rho \int_V H_\alpha \frac{\partial v_i}{\partial t} dV + \rho \int_V H_\alpha v_j v_{i,j} dV - \int_V H_{\alpha,i} p dV + \int_V \mu H_{\alpha,j} v_{i,j} dV = \int_V H_\alpha f_i^B dV + \int_S H_\alpha \left(-p n_i + \mu v_{i,j} n_j \right) dS \tag{10}$$

The chosen interpolation functions for the velocity and pressure are, respectively;

$$v_i = H_\alpha v_{i\alpha} \tag{11}$$

$$p = G_\delta p_\delta \tag{12}$$

Next, equations (11) and (12) are substituted into equations (10) and (8) to arrive at;

$$\left[\rho \int_V H_\alpha H_\beta dV \right] \dot{v}_{\beta i} + \left[\rho \int_V H_\alpha H_\gamma v_{j\gamma} H_{\beta,j} dV \right] v_{\beta i} + \left[\int_V \mu H_{\alpha,j} H_{\beta,j} dV \right] v_{\beta i} - \left[\int_V H_{\alpha,i} G_\beta dV \right] p_\beta =$$
$$\int_V H_\alpha f_i^B dV + \int_S H_\alpha \left(-p n_i + v_{i,j} n_j \right) dS \tag{13}$$

$$\left[\int_V G_\delta H_{\alpha,i} dV \right] v_{\alpha i} = 0 \tag{14}$$

Finally, the finite element matrix equation takes the form of;

$$\begin{bmatrix} \mathbf{M_v} & \mathbf{0} \\ \mathbf{0} & \mathbf{0} \end{bmatrix} \begin{Bmatrix} \dot{\mathbf{v}} \\ \dot{\mathbf{p}} \end{Bmatrix} + \begin{bmatrix} \mathbf{K_{vv}} + \mathbf{K}_{\mu v} & \mathbf{K_{vp}} \\ \mathbf{K_{vp}^T} & \mathbf{0} \end{bmatrix} \begin{Bmatrix} \mathbf{v} \\ \mathbf{p} \end{Bmatrix} = \begin{Bmatrix} \mathbf{R_B} + \mathbf{R_S} \\ \mathbf{0} \end{Bmatrix} \tag{15}$$

where, the mass, convective, viscosity, pressure gradient, volume force and surface force terms are, respectively;

$$(\mathbf{M_v})_{i\alpha\beta} = \rho \int_V H_\alpha H_\beta dV = \rho \int_V \mathbf{H}^T \mathbf{H} dV$$

$$(\mathbf{K_{vv}})_{i\alpha\beta} = \rho \int_V H_\alpha H_\gamma v_{j\gamma} H_{\beta,j} dV = \rho \int_V \mathbf{H}^T \left(\mathbf{H} \mathbf{v}_1 \mathbf{H}_{,x_1} + \mathbf{H} \mathbf{v}_2 \mathbf{H}_{,x_2} + \mathbf{H} \mathbf{v}_3 \mathbf{H}_{,x_3} \right) dV$$

$$(\mathbf{K_{\mu v}})_{i\alpha\beta} = \int_V \mu H_{\alpha,j} H_{\beta,j} dV = \int_V \mu \left(\mathbf{H}_{,x_1}^T \mathbf{H}_{,x_1} + \mathbf{H}_{,x_2}^T \mathbf{H}_{,x_2} + \mathbf{H}_{,x_3}^T \mathbf{H}_{,x_3} \right) dV$$

$$(\mathbf{K_{vp}})_{i\alpha\delta} = -\int_V H_{\alpha,i} G_\delta dV = -\int_V \mathbf{H}_{,x}^T \mathbf{G} dV$$

$$(\mathbf{R_B})_{i\alpha} = \int_V H_\alpha f_i^B dV = \int_V \mathbf{H}^T \mathbf{f}^B dV$$

$$(\mathbf{R_S})_{i\alpha} = \int_S H_\alpha \left(-p n_i + v_{i,j} n_j \right) dS = \int_S \mathbf{H}^T \left(-p \mathbf{n} + \mathbf{v}_{,x} \cdot \mathbf{n} \right) dS \tag{16}$$

Next, in order to implement the incremental-iterative procedure, the velocity and pressure at the end of each time step is defined, respectively;

$$^{t+\Delta t} v_{i\alpha} = ^{t+\Delta t} v_{i\alpha}^{(m-1)} + \Delta v_{i\alpha}^{(m)} \tag{17}$$

$$^{t+\Delta t} p_\delta = ^{t+\Delta t} p_\delta^{(m-1)} + \Delta p_\delta^{(m)} \tag{18}$$

where *(m)* is iteration. Next, by substituting equations (17) and (18) into equations (13) and (14) we obtain the incremental-iterative equations as;

$$\left[\rho\frac{1}{\Delta t}\int_V H_\alpha H_\beta dV\right]\left(\Delta v_\beta^{(m)}\right)+\left[\rho\int_V H_\alpha H_\gamma{}^{t+\Delta t}v_\gamma^{(m-1)}H_{\beta,j}dV\right]\left(\Delta v_\beta^{(m)}\right)+\left[\rho\int_V H_\alpha H_{\gamma,j}{}^{t+\Delta t}v_\gamma^{(m-1)}H_\beta dV\right]\left(\Delta v_\beta^{(m)}\right)$$

$$\left[\int_V \mu H_{\alpha,j}H_{\beta,j}dV\right]\left(\Delta v_\beta^{(m)}\right)-\left[\int_V H_{\alpha,i}G_\delta dV\right]\left(\Delta p_\delta^{(m)}\right)=\int_V H_\alpha f_i^{~B}dV+\int_S H_\alpha\left(-p\eta_i+v_{i,j}n_j\right)dS-$$

$$\left[\rho\frac{1}{\Delta t}\int_V H_\alpha H_\beta dV\right]\left({}^{t+\Delta t}v_\beta^{(m-1)}-{}^tv_\beta\right)-\left[\rho\int_V H_\alpha H_\gamma{}^{t+\Delta t}v_\gamma^{(m-1)}H_{\beta,j}dV\right]\left({}^{t+\Delta t}v_\beta^{(m-1)}\right)-\left[\int_V \mu H_{\alpha,j}H_{\beta,j}dV\right]\left({}^{t+\Delta t}v_\beta^{(m-1)}\right)- \tag{19}$$

$$\left[\int_V H_{\alpha,i}G_\delta dV\right]\left({}^{t+\Delta t}p_\delta^{(m-1)}\right)$$

$$\left[\int_V G_\delta H_{\alpha,i}dV\right]\left(\Delta v_{\alpha i}^{(m)}\right)=-\left[\int_V G_\delta H_{\alpha,i}dV\right]\left({}^{t+\Delta t}v_{\alpha i}^{(m-1)}\right) \tag{20}$$

Now equation (15) becomes;

$$\begin{bmatrix}\dfrac{1}{\Delta t}\mathbf{M_v}+{}^{t+\Delta t}\mathbf{K_{vv}}^{(m-1)}+{}^{t+\Delta t}\mathbf{K_{\mu v}}^{(m-1)}+{}^{t+\Delta t}\mathbf{J_{vv}}^{(m-1)} & \mathbf{K_{vp}} \\ \mathbf{K_{vp}^T} & \mathbf{0}\end{bmatrix}\begin{Bmatrix}\Delta\mathbf{v}^{(m)} \\ \Delta\mathbf{p}^{(m)}\end{Bmatrix}=\begin{Bmatrix}{}^{t+\Delta t}\mathbf{F_v}^{(m-1)} \\ {}^{t+\Delta t}\mathbf{F_p}^{(m-1)}\end{Bmatrix} \tag{21}$$

where the matrices and vectors are;

$$\left(\mathbf{M_v}\right)_{i\alpha\beta}=\rho\int_V H_\alpha H_\beta dV=\rho\int_V \mathbf{H}^T\mathbf{H}dV$$

$${}^{t+\Delta t}\left(\mathbf{K_{vv}}\right)_{i\alpha\beta}^{(m-1)}=\rho\int_V H_\alpha H_\gamma{}^{t+\Delta t}v_{j\gamma}^{(m-1)}H_{\beta,j}dV=\rho\int_V \mathbf{H}^T(\mathbf{H}^{t+\Delta t}\mathbf{v}^{(m-1)})\nabla^T\mathbf{H}dV$$

$${}^{t+\Delta t}\left(\mathbf{K_{\mu v}}\right)_{i\alpha\beta}^{(m-1)}=\int_V \mu H_{\alpha,j}H_{\beta,j}dV=\int_V \mu\nabla\mathbf{H}^T\nabla^T\mathbf{H}dV$$

$${}^{t+\Delta t}\left(\mathbf{J_{vv}}\right)_{j\alpha\beta}^{(m-1)}=\rho\int_V H_\alpha H_{\gamma,j}{}^{t+\Delta t}v_{i\gamma}^{(m-1)}H_\beta dV=\rho\int_V \mathbf{H}^T(\nabla\mathbf{H}^{t+\Delta t}\mathbf{v}^{(m-1)})\mathbf{H}dV$$

$$\left(\mathbf{K_{vp}}\right)_{i\alpha\delta}=-\int_V H_{\alpha,i}G_\delta dV=-\int_V \nabla\mathbf{H}^T\mathbf{G}dV$$

$${}^{t+\Delta t}\mathbf{F_v}^{(m-1)}={}^{t+\Delta t}\mathbf{R_B}+{}^{t+\Delta t}\mathbf{R_S}^{(m-1)}-\left({}^{t+\Delta t}\mathbf{K_{vv}}^{(m-1)}+{}^{t+\Delta t}\mathbf{K_{\mu v}}^{(m-1)}\right)^{t+\Delta t}\mathbf{v}^{(m-1)}-\mathbf{K_{vp}}^{t+\Delta t}\mathbf{p}^{(m-1)}$$

$${}^{t+\Delta t}\mathbf{F_p}^{(m-1)}=-\mathbf{K_{vp}}^T{}^{t+\Delta t}\mathbf{v}^{(m-1)}$$

$${}^{t+\Delta t}\left(\mathbf{R_B}\right)_{i\alpha}=\int_V H_\alpha{}^{t+\Delta t}f_i^B dV=\int_V \mathbf{H}^{T~t+\Delta t}\mathbf{f}^\mathbf{B}dV$$

$${}^{t+\Delta t}\left(\mathbf{R_S}\right)_{i\alpha}^{(m-1)}=\int_S H_\alpha\left(-{}^{t+\Delta t}p^{(m-1)}n_i+{}^{t+\Delta t}v^{(m-1)}{}_{i,j}n_j\right)dS=\int_S \mathbf{H}^T\left(-{}^{t+\Delta t}p^{(m-1)}\mathbf{n}+\nabla^{t+\Delta t}\mathbf{v}^{(m-1)}\cdot\mathbf{n}\right)dS \tag{22}$$

The left upper index $t+\Delta t$ denotes that the quantities are evaluated at the end of time step. V and S are the volume and the surface of the finite element, respectively. The matrix $\mathbf{H}$ and $\mathbf{G}$ contains the interpolation functions for the velocities and the pressure, respectively. The matrix $\mathbf{M_v}$ is mass matrix, $\mathbf{K_{vv}}$ and $\mathbf{J_{vv}}$ are convective matrices, $\mathbf{K_{\mu v}}$ is viscous matrix, $\mathbf{K_{vp}}$ is pressure matrix and $\mathbf{F_v}$ and $\mathbf{F_p}$ are forcing vectors. $\mathbf{R_B}$ and $\mathbf{R_S}$ are volume and surface forces, respectively.

3.   Results and discussion

In order to assess the accuracy of the finite element methods employed, the pulsatile flow in a typical cylindrical artery is computed and compared with the well known analytical Womersley solution [16,17]. An idealized long, straight, rigid-walled cylindrical artery with length L, and radius r, is subjected to an inflow velocity that was uniform in space and periodic in time. The time variation is described by a sinusoidal function $V(t) = \vec{V}(1 + \sin(2\pi(t/T)))$ with mean velocity, $\vec{V} = 135 mm/s$ and period, $T = 0.2s$ as shown in Figure 3.
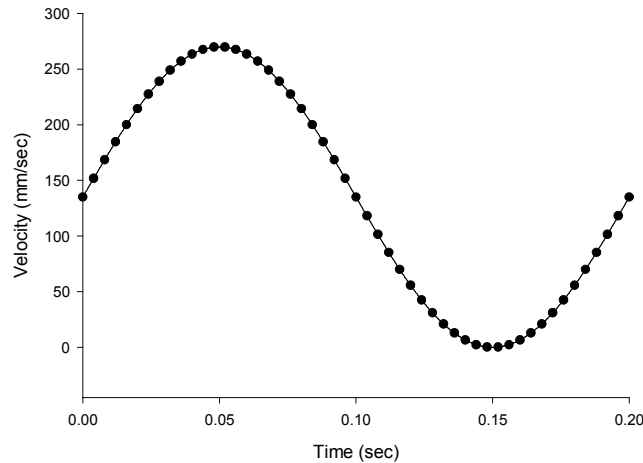
Figure 3. Sinusoidal velocity profile

A sufficient distance from the inlet, the radial and circumferential components of velocity and pressure vanish. The axial velocity becomes a function of radius only and the pressure varies linearly with axial position. Figures 4 and 5 illustrate the numerically computed axial velocities against the well known analytical solution and the velocity profiles at 4 different phases within one cardiac cycle for the flow in a long, straight, cylindrical tube i. e. t/T = 0.125, t/T = 0.375, t/T = 0.625 and t/T = 0.875, respectively. In these figures and thereafter, the blood flow direction is referred to the arrow and the various phases of the pulsatile flow are referred to the flow waveform icon within each figure. The maximum error observed between the analytical and numerical results is below 15%. Further improvements can be made by adopting a much finer mesh.
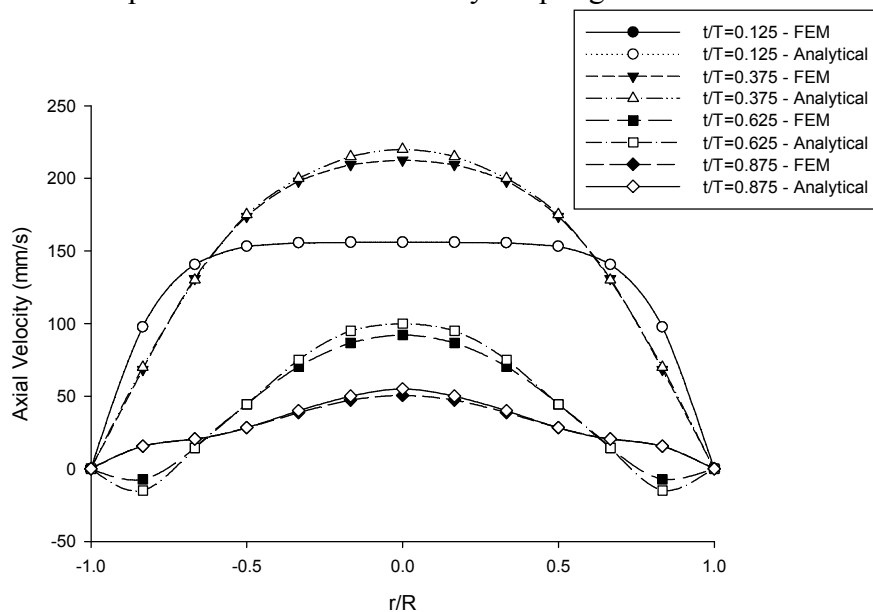

Figure 4. Theoretical and computed axial velocities at four different phases within one cardiac cycle
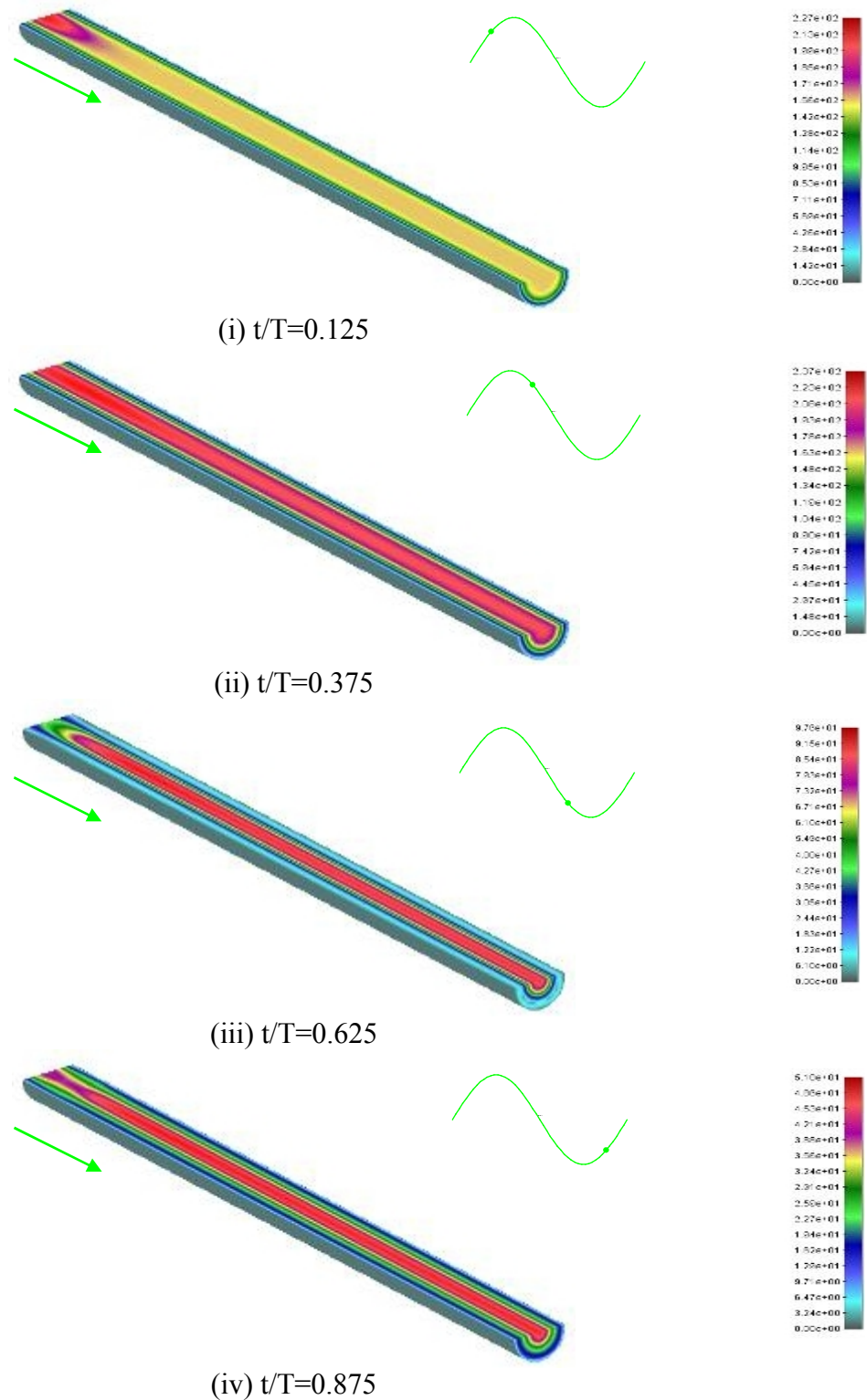
(i) t/T=0.125

(ii) t/T=0.375

(iii) t/T=0.625

(iv) t/T=0.875

Figure 5. Three-dimensional velocity contours in a long, straight cylindrical tube at four different phases within the sinusoidal waveform; (i)t/T=0.125; (ii)t/T=0.375; (iii)t/T=0.625; (iv)t/T=0.875.

Next, as a benchmark problem for flow simulation in abdominal aortic aneurysm models, we characterized the flow in a healthy infrarenal aorta. The infrarenal aorta is idealized as a straight tube of diameter d_{AA}=18mm. The model is supplied with a physiologically realistic pulsatile inflow waveform measured in a male subject at rest, as shown in Figure 1. The flow evolution was studied at six different phases of the pulsatile flow: (i) acceleration to systole, t/T=0.035 (ii) peak systole,

t/T=0.16 (iii) deceleration into retrograde flow, t/T=0.35 (iv) peak retrograde flow, t/T=0.55 (v) early diastole, t/T=0.77 and (vi) late diastole, t/T=0.87. Figures 6 and 7 show the evolution of velocity contours and vectors profiles, respectively at six different phases within the cardiac cycle.

During flow acceleration, the flow develops into the characteristic top-hat velocity profile. When the Womersley number is small, viscous forces dominate and the velocity profiles are parabolic in shape. However, for Womersley number above 10, which is the case in abdominal aorta, the unsteady inertial forces dominate, and the flow is nearly top-hat with thin boundary layers. At the peak systole, the thickness of the boundary layer scales as d_{AA}/α. After the peak systole, that is, during flow deceleration, the flow slows down along the walls and quickly reverses, while the central region bulk of the fluid in the healthy aorta moves forward with a blunt velocity profile. At peak retrograde flow, this central region bulk of fluid only reverses fully. As the flow comes out from the retrograde flow region into the early diastolic flow region, the net flow decelerates back to zero and ends up moving forward again. At late diastole, the flow relaxes to near rest before being accelerated again at the beginning of the next cardiac cycle. It is important to point out that although the flow develops an inflexional velocity profile during diastole, it remains entirely laminar during the whole cardiac cycle. The axial velocity distributions at each key step along the pulsatile flow are as illustrated in Figure 8.

This boundary layer of reversed flow close to the wall is an important characteristic of pulsatile flow. This exhibits that even for a straight section of an artery with positive volume flow, there is always some time within the cardiac cycle where the viscous traction forces are opposite the dominant flow direction. This has implications in the design of *in vitro* devices designed to replicate the shear forces on the inner wall of the artery. Namely, *in vivo*, the luminal surface is exposed to shear forces which reverse in direction for some portion of the cardiac cycle.

(i) t/T=0.035

(ii) t/T=0.16

(iii) t/T=0.35

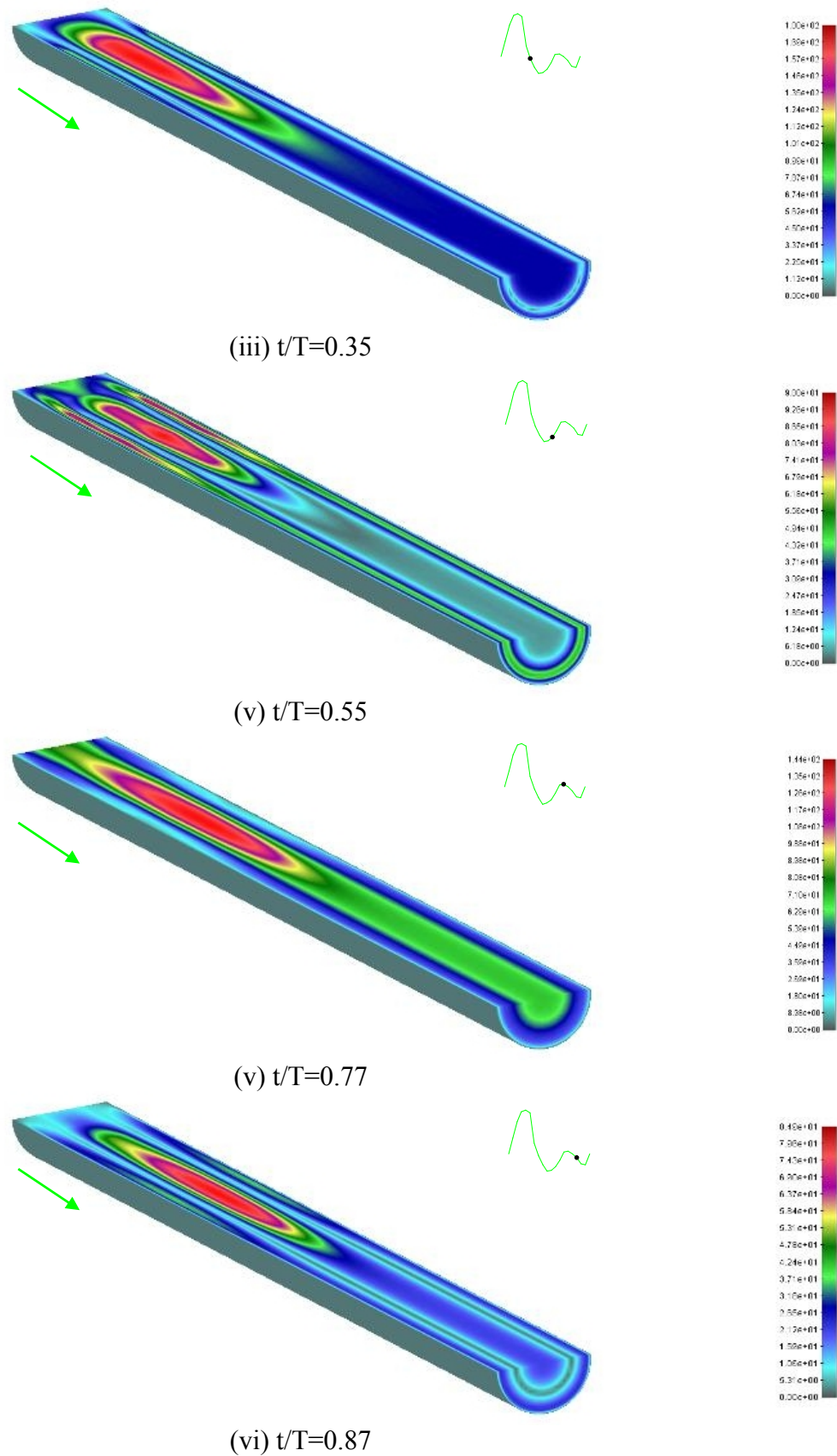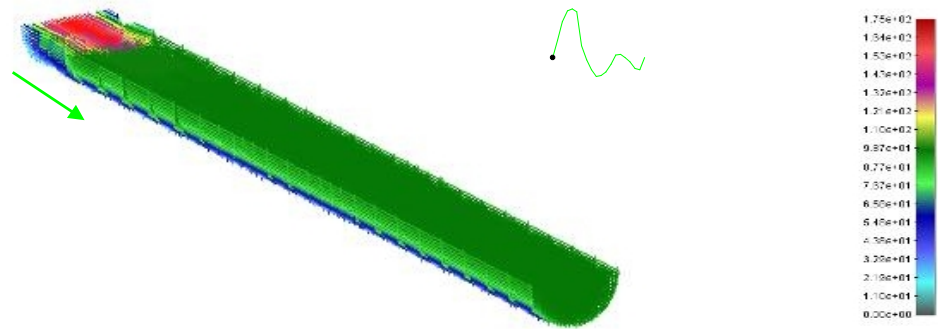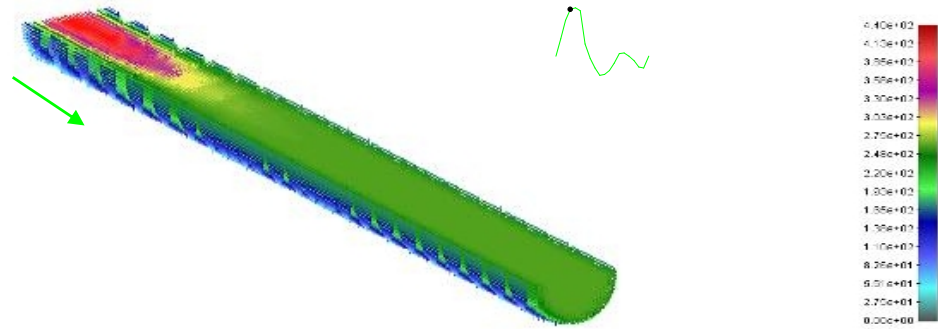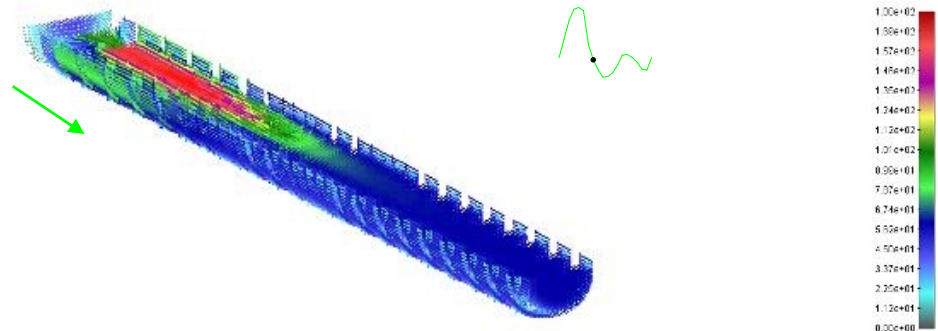(v) t/T=0.55

(v) t/T=0.77

(vi) t/T=0.87
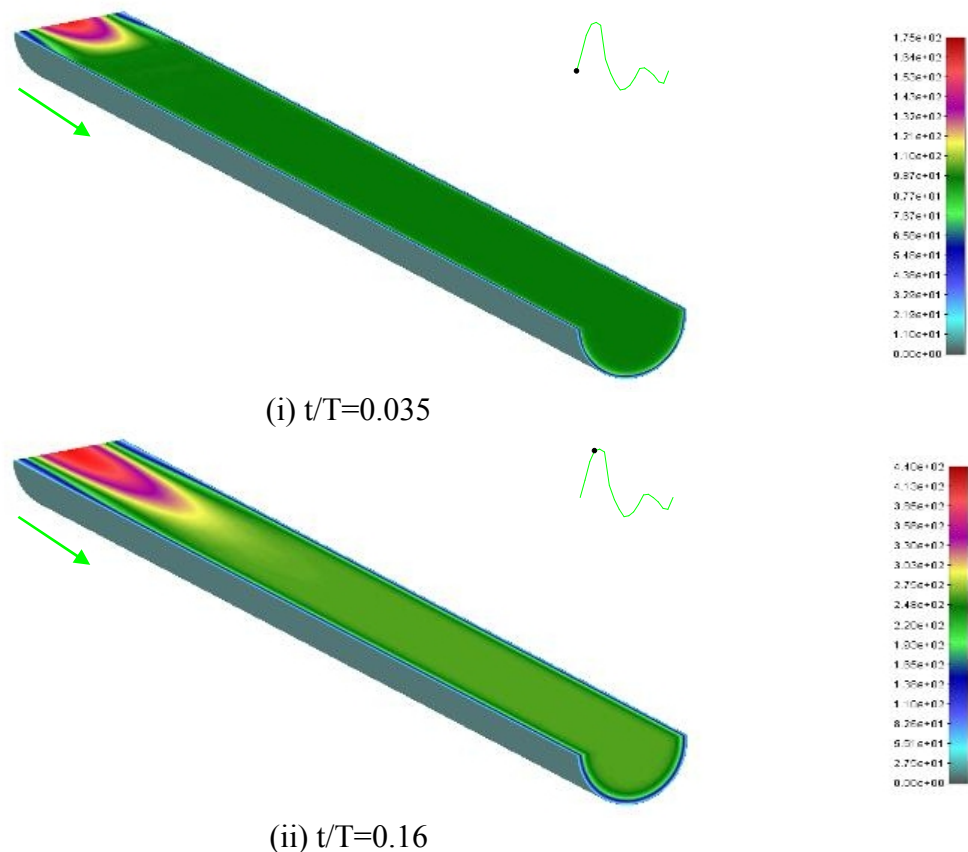
Figure 6. 3D Velocity flow contours in a healthy aorta under physiologically realistic pulsatile flow at six phases of the pulsatile flow cycle: (i) flow acceleration, t/T=0.035; (ii) peak systole, t/T=0.16; (iii) flow deceleration, t/T=0.35; (iv) peak retrograde flow, t/T=0.55; (v) early diastole, t/T=0.77; (vi) late diastole, t/T=0.87

(i) t/T=0.035
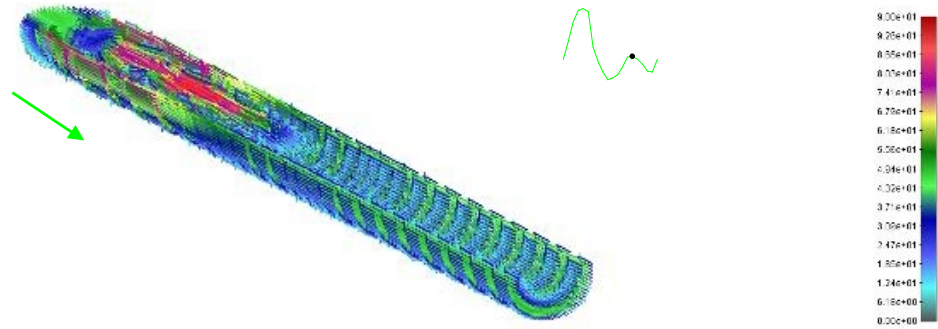

(ii) t/T=0.16

(iii) t/T=0.35

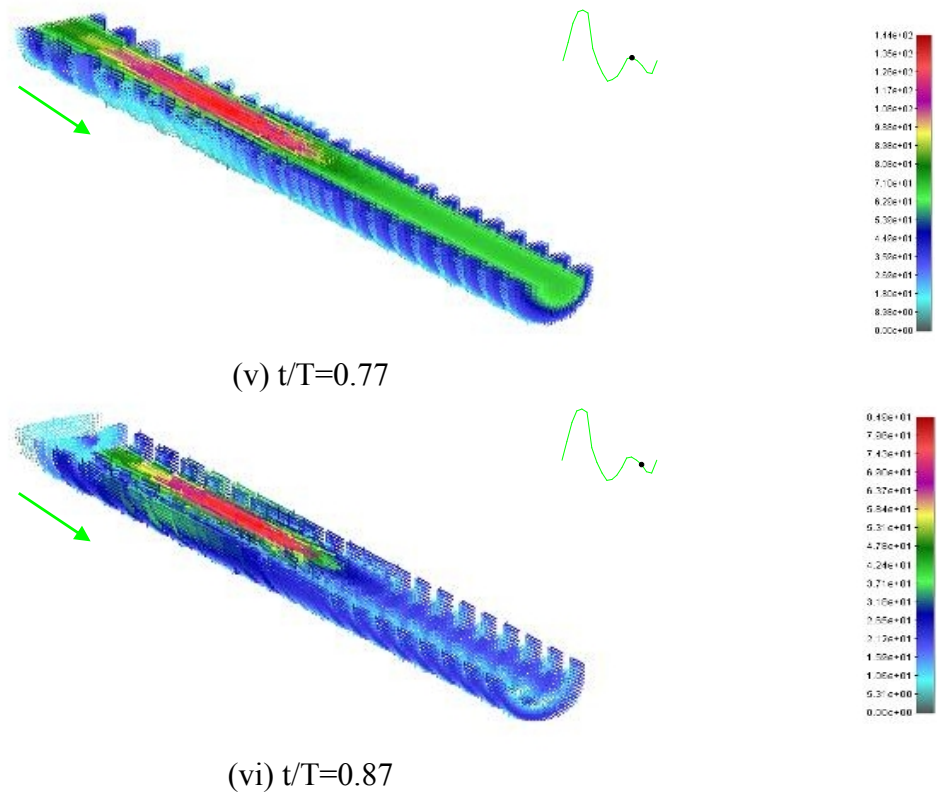(iv) t/T=0.55

(v) t/T=0.77

(vi) t/T=0.87

Figure 7. 3D Velocity vector profiles in a healthy aorta under physiologically realistic pulsatile flow at six phases of the pulsatile flow cycle: (i) flow acceleration, t/T=0.035; (ii) peak systole, t/T=0.16; (iii) flow deceleration, t/T=0.35; (iv) peak retrograde flow, t/T=0.55; (v) early diastole, t/T=0.77; (vi) late diastole, t/T=0.87
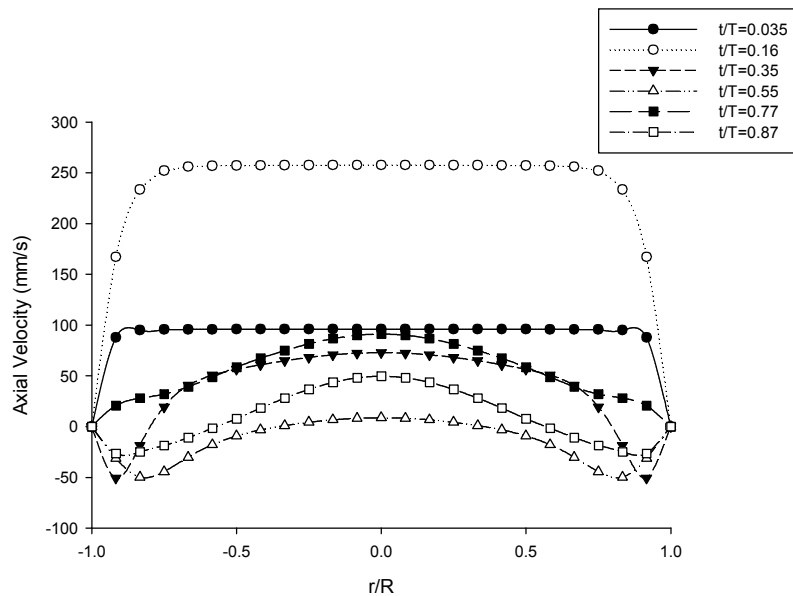

Figure 8. Axial velocity distribution of pulsatile blood flow in a healthy aorta at six different phases within one complete pulsatile flow cycle

4. Conclusion

A complete set of three-dimensional mixed velocity-pressure (v-p) finite element method was derived to solve the pulsatile nature of blood flow in a rigid-walled healthy aorta. The numerical scheme exploits the Galerkin method and the implicit incremental-iterative procedure.

The presented computational technique was used to analyze the flow dynamics in a healthy abdominal aorta under a physiologically realistic pulsatile flow at rest that can be considered as a benchmark problem. It was observed that there exists a boundary layer of reversed flow close to the wall that is considered an important characteristic of pulsatile flow. This exhibits that even for a straight section of an artery with positive volume flow, there is always some time within the cardiac cycle where the viscous traction forces are opposite the dominant flow direction. This has implications in the design of *in vitro* devices designed to replicate the shear forces on the inner wall of the artery. Namely, *in vivo*, the luminal surface is exposed to shear forces which reverse in direction for some portion of the cardiac cycle. This leads to the ability to further co-relate flow dynamics in an aneurismal aorta and subsequently allow biomedical engineers and physicians to diagnose and design patient-specific treatment plans that can improve their care. Having said this, clinical application of numerical modelling and computer-aided surgical planning is the key for the future of medicine.

Nomenclature

ρ	*Fluid density*
σ	*Fluid stress*
f	*Body force*
v	*Velocity*
p	*Fluid pressure*
μ	*Dynamic viscosity*
$\dot{e}_{ij}$	*Tensor of velocity deformation*
δ_{ij}	*Kronecker delta*
Re	*Reynolds number*
Q	*Flowrate*
α	*Womersley number*
T	*Time*

References

[1] Cotran RS, Kumar V, Robbins SL, *Robbins Pathologic Basis of Decease*, Saunders, London, 1994.

[2] Newman AB, Arnold AM, Burke GL, O'Leary DH, Manolio TA, *Cardiovascular disease and mortality in older adults with small abdominal aortic aneurysms detected by ultrasonography: the cardiovascular health study,* Annals of Internal Medicine, 2001, **134**: p. 182-190.

[3] Clement Kleinstreuer, Zhonghua Li, *Analysis and computer program for rupture-risk prediction of abdominal aortic aneurysm*, BioMedical Engineering OnLine, 2006, **5:19**.

[4] Taylor CA, Hughes TJR, Zarins CK, *Finite element modeling of three-dimensional pulsatile flow in the abdominal aorta: Relevance to atherosclerosis*, Annals of Biomedical Engineering, 1998, **26**: p. 975-987.

[5] Geneves C, Wilquem F, Treyve F, Cloutier G, Soulez G, Saidane K, *Study on non stationary mode flow of an abdominal aortic aneurysm*, Journal of Applied Biomaterials & Biomechanics, 2005, **3(3)**: p. 176-183.

[6] Filipovic N, Kojic M, *Computer simulation of blood flow with mass transport through the carotid artery bifurcation*, Journal of Theoretical & Applied Mechanics, 2004, **31(1)**: p. 1-33.

[7] Barth T, Bochev P, Gunzburger M, Shadid J, *A taxonomy of consistently stabilized finite element methods for the Stokes problem*, SIAM Journal of Scientific Computing,

2004, **25**: p. 1585-1607.

[8] Becker R, Braack M, *A finite element pressure gradient stabilization for the Stokes equations based on a local projection*, Calcolo, 2001, **38**: p. 173-199.

[9] Boachev P, Gunzburger M, *An absolute stable pressure-Poisson stabilized method for the Stokes equations*, SIAM Journal of Numerical Analysis, 2005, **42**: p. 1189-1207.

[10] Hughes T, Franca L, *A new finite element formulation for computational fluid dynamics: VII. The Stokes problems with various well-posed boundary condition: symmetric formulations that converge for all velocity pressure spaces*, Computer Methods in Applied Mechanics and Engineering, 1987, **65**: p. 85-96.

[11] Behr MA, Franca PL, Tezduyar TE, *Stabilized finite element method for the velocity-pressure-stress formulation for incompressible flows*, Computer Methods in Applied Mechanics and Engineering, 1993, **104**: p. 31-4.

[12] Filipovic N, *Numerical analysis of coupled problems: Fluid flow through porous deformable medium with implementation in biomechanics and geomechanics*, Ph. D. Thesis, University of Kragujevac, Serbia-Yugoslavia, 1996.

[13] Quarteroni A, Tuveri M, Veneziani A, *Computational vascular fluid dynamics: problems, models and methods,* Comp. Visual Sci., 2000, **2**: p. 163-197.

[14] Milnor W, *Hemodynamics*, 2nd Edition, Williams and Wilkins, Baltimore, MD, p. 34-35.

[15] Peattie RA, Riehle TJ, Bluth EI, *Pulsatile flow in fusiform models of abdominal aortic aneurysms: flow fields, velocity patterns and flow-induced wall stresses.* Journal of Biomechanical Engineering, 2005, **126**: p. 438-446.

[16] Womersley JR, *Method for the calculation of velocity, rate of flow and viscous drag in arteries when the pressure gradient is known*, J. Physiol., 1955, **127**: p. 553-563.

[17] Badreddin G, Vijayajothi P, Kahar O, Mohamed Rafiq AK, Kanesan M, *Graphical user interface (GUI) in MatLab for solving the pulsatile flow in blood vessel*, CFDLetters, 2009, **1**(1): p. 50-58.

[18] Gresho PM, Lee RL, Sani RL, *On the time dependent solution of the incompressible Navier Stokes equations in two and three dimension*, Finite Element in Fluids, **4**: Chapter 2, Gallagher et al, John Wiley & Sons, Chichester, 1982.

[19] D. Kwak, JLC Chang, SE Rogers, M Rosenfeld, *Potential applications of computational fluid dynamics to biofluid analysis*, NASA Technical Memorandum, 1988.